Current Biology 24, 2085–2096, September 22, 2014 ©2014 Elsevier Ltd All rights reserved http://dx.doi.org/10.1016/j.cub.2014.07.080

Article

The Retinal Projectome Reveals Brain-Area-Specific Visual Representations Generated by Ganglion Cell Diversity

Estuardo Robles,[1,*] Eva Laurell,[1] and Herwig Baier[1]
[1]Max Planck Institute of Neurobiology, Am Klopferspitz 18, 82152 Martinsried, Germany

Summary

Background: Visual information is transmitted to the vertebrate brain exclusively via the axons of retinal ganglion cells (RGCs). The functional diversity of RGCs generates multiple representations of the visual environment that are transmitted to several brain areas. However, in no vertebrate species has a complete wiring diagram of RGC axonal projections been constructed. We employed sparse genetic labeling and in vivo imaging of the larval zebrafish to generate a cellular-resolution map of projections from the retina to the brain.
Results: Our data define 20 stereotyped axonal projection patterns, the majority of which innervate multiple brain areas. Morphometric analysis of pre- and postsynaptic RGC structure revealed more than 50 structural RGC types with unique combinations of dendritic and axonal morphologies, exceeding current estimates of RGC diversity in vertebrates. These single-cell projection mapping data indicate that specific projection patterns are nonuniformly specified in the retina to generate retinotopically biased visual maps throughout the brain. The retinal projectome also successfully predicted a functional subdivision of the pretectum.
Conclusions: Our data indicate that RGC projection patterns are precisely coordinated to generate brain-area-specific visual representations originating from RGCs with distinct dendritic morphologies and topographic distributions.

Introduction

Understanding how the visual system directs diverse behaviors will require a comprehensive map of the connections between retinal ganglion cells (RGCs) and retinorecipient brain regions. RGC subtypes have previously been classified using criteria that include functional response properties, genetic markers, and dendritic morphology [1–6]. These and numerous other studies have led to the consensus view that vertebrate retinas contain approximately 20 distinct RGC types that encode specific visual features [7]. Despite these insights, the organizing principles that govern information transfer from the retina to visual brain areas remain poorly understood. For example, although differences in axonal projection targets have been shown to distinguish subsets of direction-selective RGCs [8–10], such analysis has not been extended to the complete retinal projection of any species.

Vertebrate visual systems contain several identified retinorecipient brain regions: more than 20 in mammals [11, 12] and 11 in adult teleost fish [13, 14]. Several lines of evidence suggest that RGC projections are complex and precisely regulated to generate brain-area-specific representations of visual space. For instance, a subset of visual brain regions are known to receive inputs from RGCs with specific response properties [11, 15]. Single RGCs can also innervate multiple different brain regions via axon collaterals [16–19], suggesting that parallel processing of visual information requires cell-type-specific patterns of axon branching. Furthermore, multiple brain areas are known to receive topographically biased retinal input [13, 20]. A comprehensive analysis of single RGC axonal projections will reveal how these system-wide design features are implemented at the cellular level.

We therefore set out to construct the first RGC projectome, a complete map of connections between the retina and the brain. The larval zebrafish is a genetically and optically tractable model organism well suited for this undertaking. RGC morphology can be imaged in living larvae, and genetic methods to sparsely label RGCs are well characterized [21, 22]. In addition, zebrafish larvae contain a visual system that resembles the adult in its anatomical complexity, i.e., the number of RGC types [21, 23, 24] and the number of visual brain areas [13, 25].

Systematic analysis of 446 individual RGCs identified 20 stereotyped projection patterns in the brain and successfully predicted a functional subdivision of the pretectum. The majority of these projection classes form axon arbors in multiple arborization fields (AFs), demonstrating that signal divergence via axon branching is a general organizing principle of vertebrate visual systems. Combining this projection analysis with an RGC classification based on dendritic stratification identified more than 50 structural RGC types with unique combinations of axonal and dendritic morphologies. This indicates that axonal projection pattern is a major determinant of RGC structural diversity, potentially allowing RGCs with similar response properties to mediate distinct visual behaviors. Moreover, each visual brain area receives a unique representation of visual space determined by its exact combination of RGC inputs. These cell-type-specific projection patterns are determined by both dendritic morphology and cell body position in the retina. Together, these findings represent the first comprehensive analysis of connectivity between the retina and brain of a vertebrate.

Results

Combining Genetic Axon Labeling with a Presynaptic Marker Identifies Ten RGC Arborization Fields

RGC axons in the larval zebrafish exit the eye through the optic nerve, cross the midline at the optic chiasm, and arborize in distinct AFs, which correspond to the neuropil areas of retinorecipient brain nuclei. As an anatomical reference, we constructed a 3D model of the AFs using transgenic larvae in which all RGCs express membrane-targeted mCherry to label the optic tract and the presynaptic marker synaptophysin-EGFP (Syp-GFP; Figures 1A and 1B). In addition to dense labeling of the optic tectum, clouds of Syp-GFP puncta were observed at several discrete sites along the optic tract (Figure 1C and Movie S1 available online). Each of these extratectal AFs has a distinct position relative to the following optic tract landmarks: the optic chiasm; the anterior, medial, and posterior branches formed in the thalamus; and the optic

*Correspondence: erobles@neuro.mpg.de

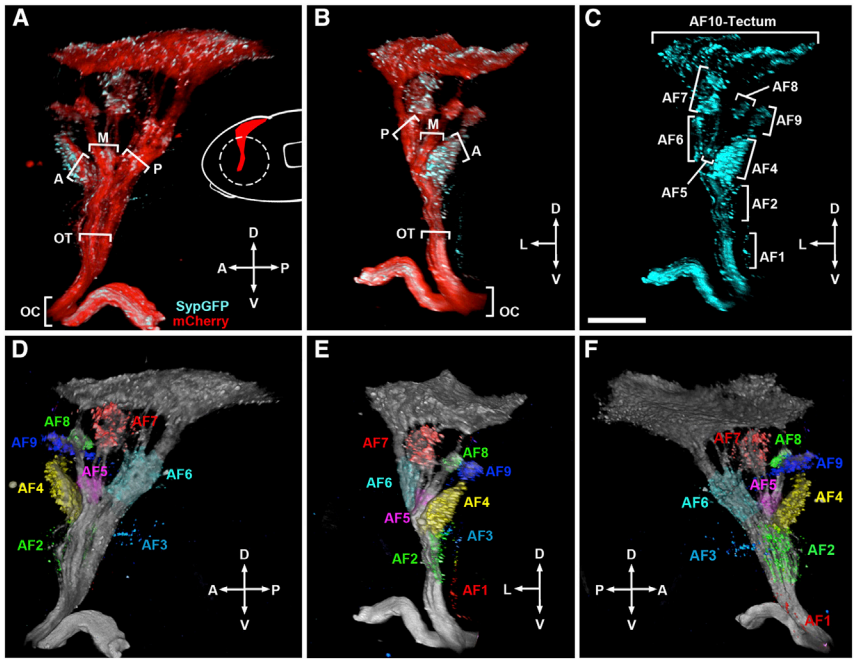

Figure 1. 3D Model of Arborization Fields Formed by RGC Axons

(A) 3D reconstruction of a fixed 6 dpf larval brain with RGC expression of membrane-targeted mCherry (red) and Syp-GFP (cyan) driven by atoh7:Gal4 driver transgene. Note the optic chiasm (OC), main bundle of the optic tract (OT), and anterior (A), medial (M), and posterior (P) branches formed in the thalamus. The inset shows a schematic side view of larva and removal of the contralateral eye (dashed line) to reveal the optic tract.

(B) Frontal view of volume in (A). Note distinct mediolateral position of OT branches.

(C) Syp-GFP channel of volume in (B). Brackets indicate distinct arborization fields formed by RGC axons. Note that AF3 is located in a plane behind AF2 in this view.

(D–F) Lateral, frontal, and medial views of volume in (A)–(C) with AF1–AF9 pseudocolored in the Syp-GFP channel and overlaid on the mCherry signal in gray. Note that each AF has a distinct position along both the anteroposterior and mediolateral axes.

The scale bar represents 50 μm. See also Movie S1.

tectum (Figures 1A and 1B). The location of these regions relative to the optic tract was consistent with AFs previously described in the larval zebrafish [25] (Figures 1D–1F). We therefore used Burrill and Easter's nomenclature, numbering the AFs according to their proximity to the optic chiasm from 1 to 10, with AF10 being the neuropil of the optic tectum.

Sparse Mosaic Labeling Reveals the Morphologies and Projection Targets of Individual RGC Axons

To map retinal projections with single-cell resolution, we utilized two distinct mosaic labeling approaches. The first is a highly variegated UAS:mGFP reporter, BGUG [22], used in conjunction with pan-RGC transgenic gal4 driver lines. In a second approach, two- to eight-cell-stage embryos transgenic for both a pan-RGC gal4 driver and UAS:mCherry reporter were injected with UAS:EGFP DNA. Both techniques restrict EGFP expression to <1% of RGCs (Figure 2A), which is essential for morphological analysis of individual RGC axonal projections (Figures 2B–2E) and dendritic stratification patterns in the retina (Figures 2F and 2G).

Preliminary examination of individual axon morphologies revealed that innervation of extratectal AFs (AF1–AF9) occurred via axon collaterals, interstitial branches formed by axons within the optic tract. We therefore used the AF location of collateral arborizations as our principal classification criteria for axonal projections. Pan-RGC mCherry expression in each larva provided stereotyped anatomical landmarks for accurate AF annotation (Figure 1). Every axon was imaged through the entire extent of the optic tract and semiautomatically segmented to identify and measure each collateral arbor along its length (Figure 2B and Table S1). Axons were scored as innervating an AF if they formed an arbor with a minimum branch length of 15 μm within the AF volume. To confirm that arbors formed by axon collaterals in extratectal AFs contain increased densities of presynaptic specializations, we imaged single RGC axons expressing DsRed and Syp-GFP (Figure S1). This analysis confirmed that collateral AF arbors contain high densities of presynaptic puncta compared to unbranched axonal segments (0.129 ± 0.025 puncta/μm versus 0.017 ± 0.01 puncta/μm, $p = 0.005$, $n = 5$ axons).

Previous studies have shown that RGC axons in the tectum form planar arbors that are restricted to a single sublamina of the tectum [21, 22]. We assigned axons innervating the tectum to one of nine sublaminar divisions: stratum opticum (SO), one of six subdivisions of the stratum fibrosum et griseum (SFGS1–SFGS6), stratum griseum centrale (SGC), or a layer at the boundary between the stratum album centrale and the stratum periventriculare (SAC/SPV) [21]. Tectal lamination was determined by analyzing the axonal stratification profile relative to mCherry labeling of the retinotectal neuropil layers (Figures 2C–2E). Including extratectal AFs (AF1–AF9) and tectal sublaminae, this makes 18 potential RGC innervation sites in the larval brain.

RGCs Form 20 Stereotyped Axonal Projection Patterns in the Brain

Analysis of 446 individual RGC axons allowed us to identify 22 projection classes (PCs) innervating unique combinations of AFs. Twenty of these classes were observed in multiple specimens, while two of these patterns were observed only once (PC21–PC22; Figure 3N). We cannot determine whether these two cases represent extremely rare classes, developmental errors, or rare instances in which axons in one of the more common projection classes formed en passant synapses in an AF without forming a collateral. Further analysis was restricted to the >99% of RGCs that formed 20 stereotyped projection classes. A subset of projection classes, illustrating the range of morphological complexity and AFs innervated, are presented in Figures 3B–3M (example images of all other projection classes are provided in Figure S2). It should be noted that we did observe variability in the fine structure of axons belonging to the same projection class (e.g., collateral arbor size and complexity; Figure S3 and Table S1). The combination of innervation sites targeted by each projection class is summarized by the connectivity matrix in Figure 3N, in which connections are weighted based on relative arbor length

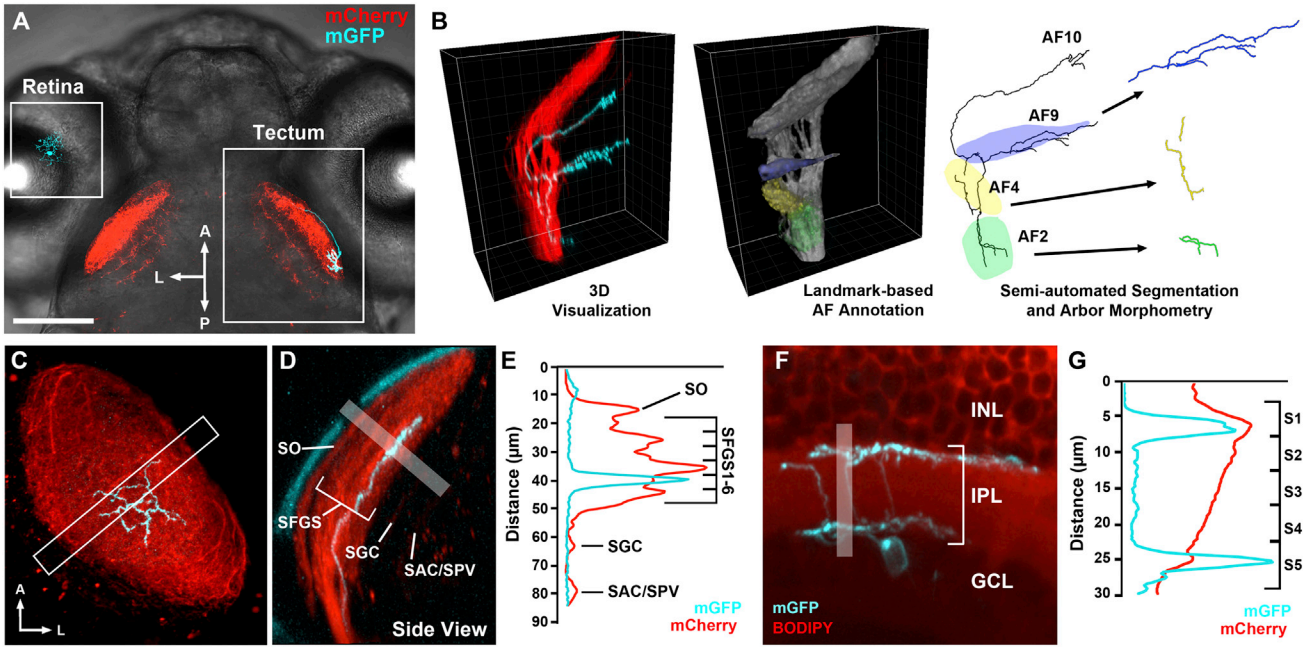

Figure 2. Workflow for In Vivo Analysis of RGC Axon and Dendrite Morphologies

(A) Low-magnification confocal image of a 7 dpf larva with a GFP-expressing RGC in the left retina projecting its axon to the contralateral tectum.

(B) 3D rendering of a single GFP-expressing axon within an optic tract labeled by mCherry. An equivalent view of the AF model presented in Figure 1 is shown. Only extratectal AFs innervated by RGC axon in left panel are color coded (AF2, AF4, and AF9). Optic tract landmarks were provided by mCherry signal. GFP fluorescence in axon was used to segment and skeletonize the axon for semiautomated morphometric analysis.

(C) Dorsal view of a mCherry labeled tectum containing a single GFP-labeled RGC axon.

(D) Cross-sectional view of subregion indicated by white box in (C).

(E) Fluorescence intensity profile along region indicated by semiopaque white bar in (D). A discrete peak in GFP signal relative to mCherry labeling of all retinotectal laminae assigned this axon to SFGS5.

(F) Maximum projection of a GFP-expressing bistratified RGC in a *roy* mutant larva.

(G) Fluorescence intensity profile along region indicated by semiopaque white bar in (F). Note the two discrete peaks in S1 and S5 sublaminae.

Scale bars represent 100 μm (A), 50 μm (C and D), and 25 μm (F). See also Figure S1.

within each innervation site (the raw data used to generate this table are presented in Table S1). Given the strong correlation between synapse formation and axon branch stabilization in developing zebrafish RGCs [26], total arbor length reflects the spatial distribution of synaptic contacts formed within each innervation site.

The Vast Majority of RGC Axons Terminate in the Tectum

One basic organizing principle revealed by single-cell projection mapping is the overwhelming predominance of axons that innervate the tectum. More than 97% of the analyzed RGC axons terminated in the tectum, while the remainder terminated in AF9 (Figure 3N; PC15). Consequently, AF1–AF8 are comprised entirely of axon collaterals formed by axons that terminate in the tectum or AF9. These single-cell projection data confirm reports in amphibians [17, 19], rodents [27], and rabbits [28], all of which suggested that the vast majority of RGCs in these species terminate in the tectum or superior colliculus (SC), the mammalian homolog of the tectum. This suggests that the tectum and SC play prominent roles in parallel processing strategies that are conserved in visual systems of both cold-blooded vertebrates and nonprimate mammals.

Parallel Innervation of Multiple Brain Areas Is Generated by Projection-Class-Specific Patterns of Axon Branching

Single-cell projection mapping allowed us to construct a wiring diagram of RGC projections to the 18 RGC innervation sites in the larval brain (Figure 3O). RGCs exhibited considerable diversity in projection complexity, ranging from axon classes that exclusively innervated one sublamina of the tectum (PC1, PC3, and PC5–PC9) to those that formed multiple branches to innervate a total of six different AFs (PC20). The majority of projection classes (13 out of 20) targeted more than one AF and these classes represent 41% of all RGCs, confirming a prominent role for signal divergence in visual information transfer to the brain. To quantitatively assess the divergence of inputs received by different innervation sites, we defined a metric, the input divergence index (IDI), which reflects the number of areas innervated by all inputs to a given site. For example, the SFGS2–SFGS5 layers of the tectum, which are only innervated by dedicated inputs, have IDI values of 0, whereas AF1 and AF3, which only receive inputs from axons that innervate at least four AFs in total, have IDI values $\geq$0.8 (Figure 3O). Overall, 14 of the 18 RGC innervation targets receive shared inputs and have IDI values >0.3. These findings demonstrate that parallel distribution of visual inputs to multiple brain regions via axon collaterals is a fundamental organizing principle of the zebrafish visual system.

One feature of tectal organization revealed by systematic projection mapping is the laminar segregation of inputs based on their innervation complexity. As discussed above, SFGS2–SFGS5 are exclusively innervated by tectum-dedicated inputs (PC5–PC8; Figures 3F and S2). In contrast, SO and SFGS1 each receive tectum-dedicated inputs, as well as inputs

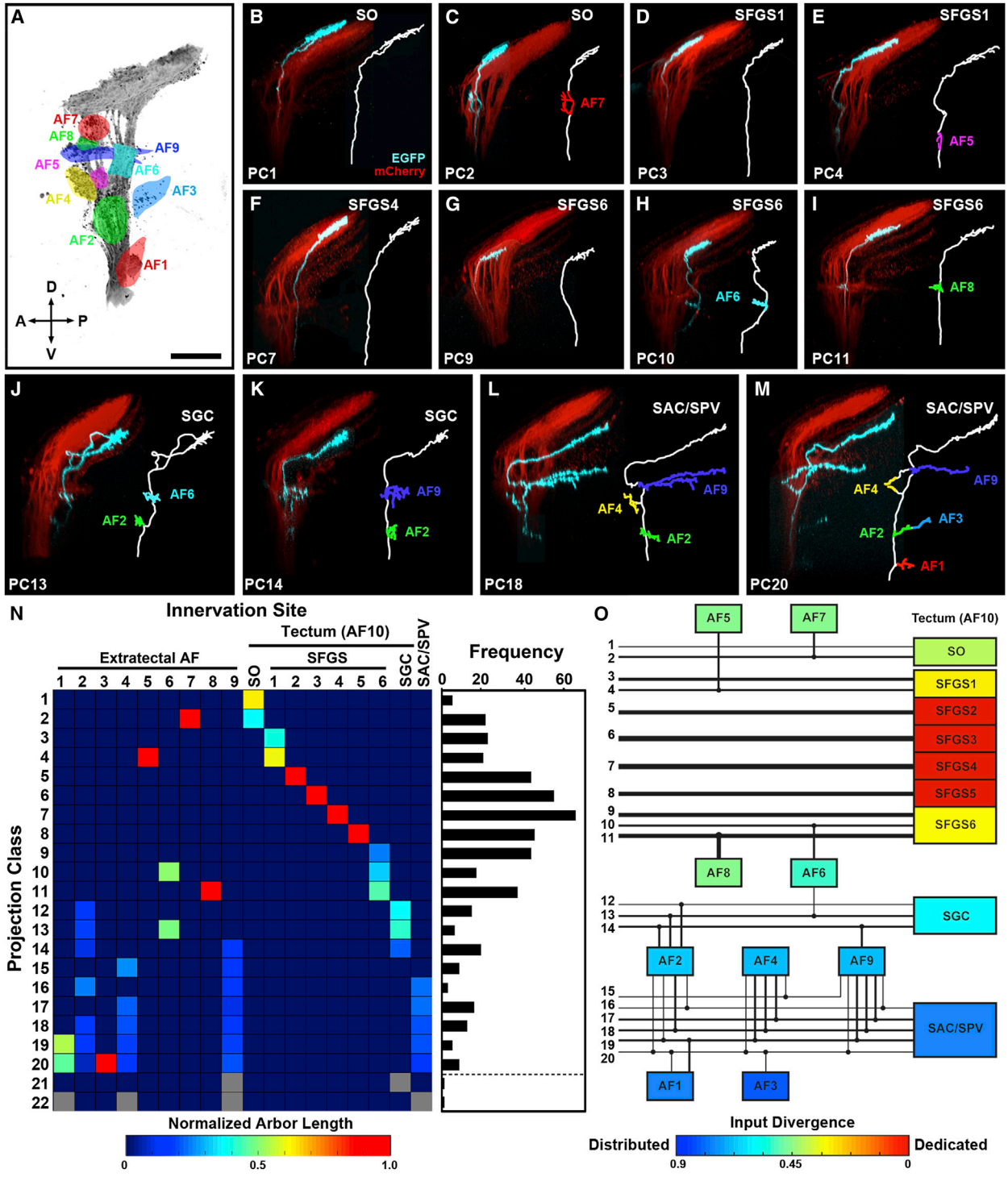

Figure 3. Stereotyped RGC Axonal Projection Patterns

(A) Schematized lateral view of optic tract and AFs.

(B–M) Representative lateral views of RGCs from 12 PCs. 3D renderings are presented alongside line tracing of axon with extratectal AF collaterals color coded according to (A). Projection patterns that innervate a single layer of the tectum are shown in (B), (D), (F), and (G). Axons that form one collateral arbor in the indicated extratectal AF are shown in (C), (E), (H), and (I). Complex axonal projection patterns that targeted three to six AFs are shown in (J)–(M). Scale bars represent 50 μm.

(N) Connectivity matrix summarizing each PC observed and its unique combination of innervation sites. Weights for each connection reflect relative arbor length within each innervation site, such that each column sums to 1. PCs observed once and not included for quantification are indicated by gray fill. Frequency distribution for each PC is presented in the right panel. Dashed line indicates cutoff for PCs with $n \geq 3$.

(O) Wiring diagram of the larval zebrafish optic tract with 20 stereotyped projection classes represented by horizontal lines. Line width represents relative frequency, and black circles indicate axonal branch points. Innervation site coloring is based on IDI values.

See also Figures S2 and S3, and Table S1.

distributed to one extratectal AF (AF7 and AF5, respectively; PC2 and PC4; Figures 3C and 3E). Similarly, the SFGS6 sublamina receives tectum-dedicated input (PC9; Figure 3G), as well as inputs from two projection classes that additionally innervate AF6 and AF8 (PC10 and PC11; Figures 3H and 3I). In contrast, the deeper layers of the tectum, SGC and SAC/SPV, do not receive any dedicated retinal inputs. RGCs that terminate in SGC each innervate at least one extratectal AF and form three projection classes: one that innervates AF2 (PC12; Figure S2), a second that innervates AF2 and AF6 (PC13; Figure 3J), and a third that innervates AF2 and AF9 (PC14; Figure 3K). The SAC/SPV sublamina is innervated by five projection classes, with each innervating at least two other AFs: AF2 and AF9 (PC16; Figure S2); AF4 and AF9 (PC17; Figure S2); AF2, AF4, and AF9 (PC18: Figure 3L); AF1, AF2, AF4, and AF9 (PC19; Figure S2); and AF1, AF2, AF3, AF4, and AF9 (PC20; Figure 3M). Together, these findings identify a general organizational plan for retinotectal input: SFGS2–SFGS5 receive tectum-specific information, SO and SFGS1 and SFGS6 integrate both tectum-specific inputs and those shared with one extratectal AF, and SGC and SAC/SPV receive only inputs distributed to three or more AFs.

Dendritic Stratification Patterns Define 14 Morphological Classes of RGCs

To examine the dendritic morphology of RGCs after axonal projection analysis, we utilized two distinct strategies. A subset of larvae used were *roy*$^{-/-}$ mutants that lack iridophores, which permits direct examination of RGC dendritic morphology in living larvae [29]. In these cases, larvae were reoriented after optic tract imaging in order to image the contralateral eye. Arbor position within the retinal inner plexiform layer (IPL) was determined by analysis of the dendrite arbor stratification profile (Figures 2F and 2G). However, live imaging of RGC dendrite morphology was not possible when an RGC was located directly behind the lens. To prevent underrepresentation of RGCs in this region, we obtained most data from larvae in which dendritic morphology was examined via retrospective GFP immunofluorescence in fixed tissue sections (Figure S4).

To develop a RGC classification based on dendritic stratification pattern in the IPL, we analyzed a separate collection of 178 individual RGCs imaged in vivo in *roy*$^{-/-}$ mutant larvae at 6–7 days postfertilization (dpf; Figure S6). Our primary classification criterion was dendrite stratification profile in the IPL, which constrains potential bipolar and amacrine cell inputs onto an RGC [30] and strongly correlates with the response properties of identified RGC types [4]. The IPL was subdivided into the sublaminae previously described in pan-RGC labeling experiments in the zebrafish (S1–S5) [29, 31]. Based on differential innervation by ON and OFF bipolar cells, distal IPL laminae (S1 and S2) are conventionally designated as "OFF" layers, whereas proximal laminae (S3–S5) are designated as "ON" layers.

Previous studies in larval zebrafish have identified four major classes of RGCs based on dendrite stratification pattern: monostratified, bistratified, multistratified, and diffuse/nonstratified [21, 23]. Analysis of laminar position within the IPL allowed us to subdivide monostratified RGCs into four subclasses: M1 OFF monostratified RGCs arborize in the S1 sublaminae, M3 ON monostratified RGCs arborize in S5, and M2 monostratified RGCs that arborize in the intermediate IPL (Figures 4A–4C and 4N). An additional monostratified ON RGC, M4, forms an arbor in S5 that also contains filopodia-like protrusions into S3 and S4 (Figures 4D and 4N). Stratification position also identified five classes of bistratified RGCs. Each forms dendritic arbors in two distinct sublaminae of the IPL (Figures 4E–4H, 4N, and S5). RGCs with diffuse/nonstratified dendrites were subdivided into two distinct subclasses. D1 cells form diffuse, nonstratified dendrites spanning all layers of the IPL (Figures 4I and 4N), whereas D2 RGCs form a diffuse dendritic arbor restricted to S3–S5 ON IPL sublayers (Figures 4J and 4N). RGCs with multistratified dendrites also formed two distinct subclasses. D3 RGCs form a compact arbor predominantly targeted to S2, S3, and S5, and a longer, asymmetric branch in S1 (Figures 4K and 4N). D4 RGCs form an asymmetric arbor with three arborizations in S1, S3, and S5 (Figures 4L and 4N). The most infrequent morphology was a biplexiform (BPL) RGC with dendrites that extend through the IPL and inner nuclear layer to terminate in the outer plexiform layer (Figures 4M and 4N). Similar BPL RGCs have been described in both mammals and other teleosts [32, 33]. In summary, we have used live imaging of dendritic stratification to define 14 subclasses of RGCs with clearly distinguishable morphological features that are likely to reflect unique complements of intraretinal inputs.

The Retina Contains More Than 50 Stable RGC Types with Distinct Combinations of Axonal and Dendritic Morphologies

Classification of the axonal and dendritic morphologies of 446 individual RGCs allowed us to examine correlations between these structural features. This analysis can directly assess to what extent visual channels formed by RGCs with similar retinal morphologies are transmitted to the same brain regions. Our data revealed a total of 82 distinct RGC types that contained unique combinations of axonal and dendritic morphologies (Figure 5A; the raw data used to generate this table are presented in Table S2). Seventy-three of these structural RGC types were observed at least twice, while 53 were observed in at least three separate specimens. With analysis restricted to these 53 structural RGC types, RGC dendritic classes gave rise to between one and eight distinct projection classes, with an average of 3.8 projection patterns per dendritic class. These findings reveal an unexpected degree of RGC diversity generated by complex patterns of axonal and dendritic differentiation.

There is evidence that RGCs in mammals form precise connections by shedding axonal collaterals [34]. Therefore, it is possible that the complex projection patterns that we have described represent immature RGCs destined to be remodeled into simpler morphologies. To examine this possibility, we conducted multiday time-lapse imaging of RGC axons with multiple AF arbors. In every instance (n = 30), projection patterns were stable throughout early larval development (6–12 dpf; Figure S6). Similarly, multiday time-lapse imaging in the retina confirmed that RGC dendritic morphology is also stable during this developmental period (n = 25; Figure S6). Therefore, these complex morphologies do not merely represent a transient stage of exuberant axonal and/or dendritic growth. Similar RGC morphologies have been observed in adult teleost fish [20, 24, 32], suggesting that this cell-type diversity may be conserved in the adult visual system.

Tectal Laminae and Extratectal AFs Receive Inputs from Unique Combinations of RGC Dendritic Types

Correlation of axonal and dendritic morphologies revealed quantitative differences in the visual inputs received by

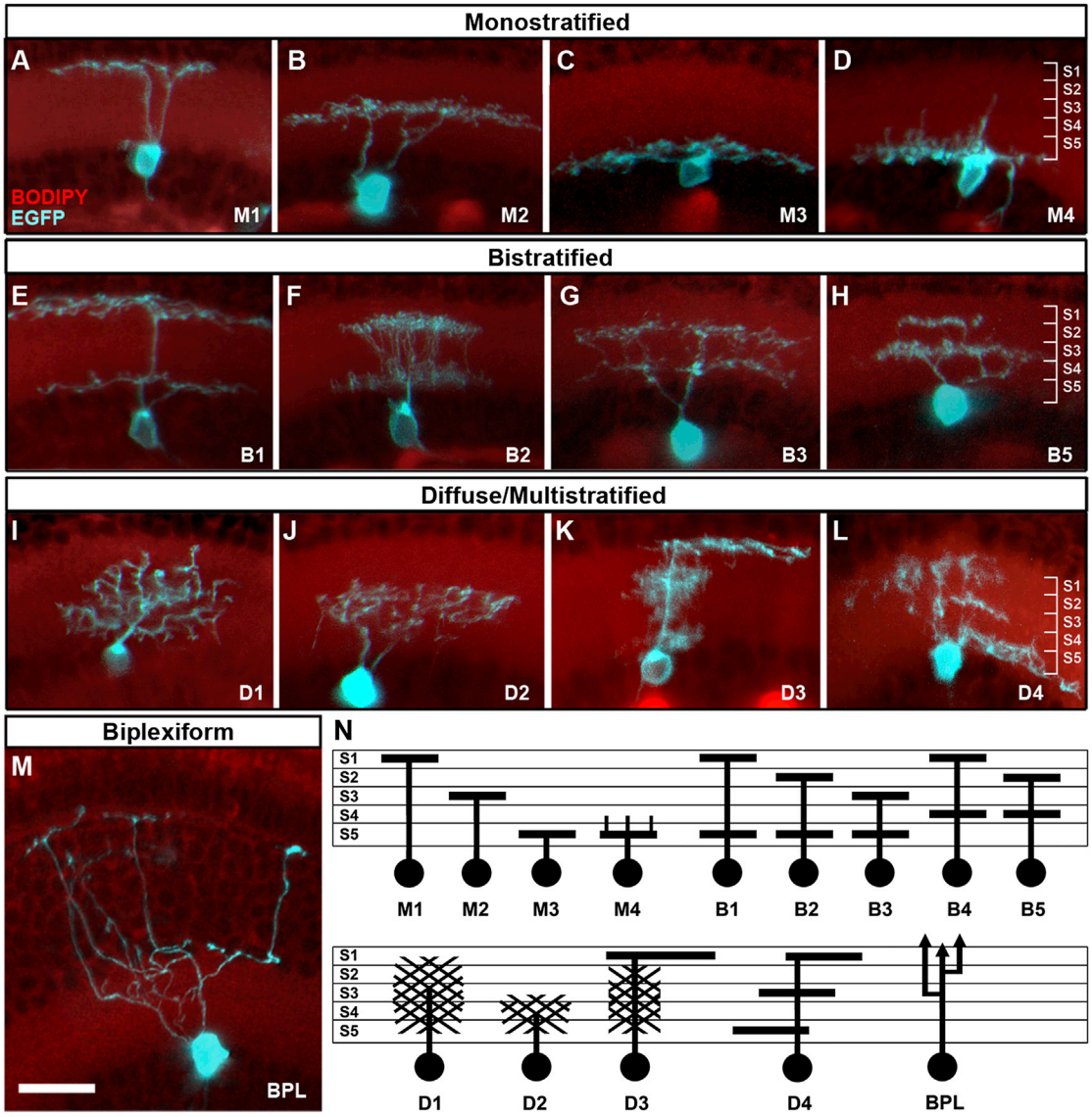

Figure 4. RGC Classification Based on Dendritic Stratification Patterns

(A–D) Monostratified RGCs with arbors targeting the OFF (A), intermediate (B), or ON (C) layers of the IPL. An additional monostratified ON RGC class forms apical dendritic branches in S3 and S4 (D).

(E–H) Example images of four of the five bistratified RGC types. Note the distinct stratification depth for both arbors.

(I–L) RGCs with diffuse dendritic arbors spanning more than two IPL layers.

(M) Biplexiform RGCs form dendrites that span the INL to reach the OPL.

(N) Schematic summary of 14 RGC classes defined by IPL stratification.

The scale bar represents 12.5 μm. See also Figures S4 and S5.

different tectal laminae. PC3–PC8, which terminate in SFGS1–SFGS5 and are largely comprised of tectum-specific inputs, exhibit a higher degree of input heterogeneity than all other projection classes (Figure 5A). Each projection class terminating in SFGS1–SFGS5 is comprised of, on average, 6.5 different dendritic classes, whereas projection classes terminating in all other tectal laminae or AF9 are, on average, innervated by 2.9 dendritic classes. In particular, the SO, SGC, and SAC/SPV layers received the most homogeneous inputs from, on average, 2.4 dendritic classes. Therefore, although the visual inputs channeled to the SO, SGC, and SAC/SPV tectal sublaminae are distributed to multiple AFs, each of these channels contains a lower diversity of input types.

Although our findings indicate that the majority of projection classes (19 of 20) originate from multiple dendritic classes of RGCs, we did observe strong trends in the dendritic morphologies of RGCs that project to specific AFs or tectal sublaminae. For example, within the six projection classes that terminate in AF9 or SAC/SPV, 72% of these RGCs have dendrites restricted to the innermost ON layers of the IPL (PC15–PC20; M3, M4, and D2; Figure 5A). In contrast, SGC-terminating projection classes were entirely comprised of M1 monostratified OFF RGCs and B1 bistratified RGCs, which contain a dendrite in the outermost OFF layer of the IPL (PC12–PC14; Figure 5A). Examination of the dendritic classes that innervate specific AFs, irrespective of projection class, revealed that each AF

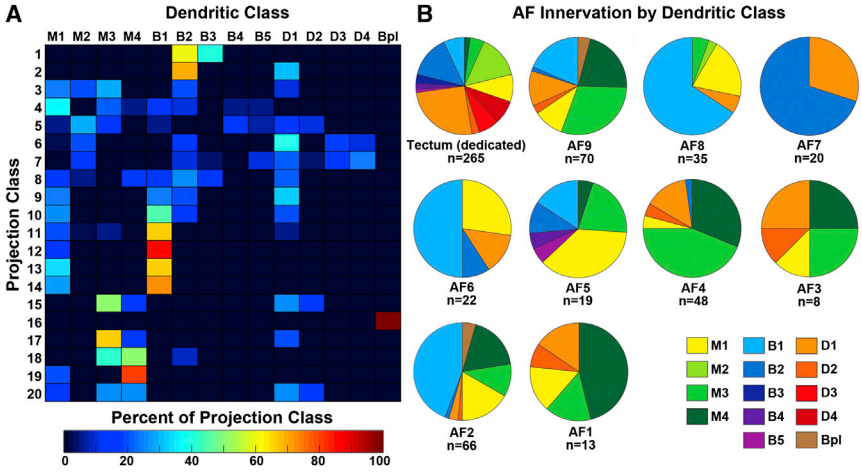

Figure 5. Complex Patterns of Axonal and Dendritic Structural Differentiation Generate Brain-Area-Specific Visual Representations

(A) Contribution of RGCs with specific dendritic morphologies to each axonal projection pattern. Each row sums to 100%. Eighty-two colorized squares represent distinct RGC populations with unique combinations of dendritic and axonal morphologies. Seventy-five of these were observed in multiple specimens.

(B) Quantification of relative contributions of specific dendritic classes to each AF.

See also Figure S6 and Table S2.

receives a unique combination of retinal inputs. Although several AFs received inputs from similar complements of dendritic classes (AF1, AF3, and AF4; AF6 and AF8; Figure 5B), in each instance the relative proportions of these inputs was area specific. Notably, a subset of AFs also received major input from a single dendritic class. AF7 receives a majority of its input from B2 RGCs, while AF6 and AF8 are both predominantly innervated by B1 RGCs (50% and 65.7%, respectively).

Cell-Type-Specific Projection Patterns Generate Biased Visual Maps throughout the Brain

A central goal of this study was to gain insight into how system-wide design principles of the visual system are implemented at the cellular level. RGC axons have been shown to form retinotopically biased visual maps in visual brain centers [13, 20]. Biased visual maps in the brain could be formed by entire RGC dendritic classes that are asymmetrically distributed in the retina. Alternatively, distinct projection patterns could be specified within topographically restricted subsets of RGC classes that are, as a whole, uniformly distributed throughout the retina.

To determine which AFs receive biased retinal input and thereby identify projection classes that originate from nonuniformly distributed RGCs, we performed local injections of the lipophilic dyes DiI and DiD into either dorsal and ventral (Figures 6A and 6B) or nasal and temporal (Figures 6C–6D and Movie S2) hemiretinae of fixed larvae. As expected, retinal projections to the tectum exhibited uniform retinotopy: nasal, temporal, dorsal, and ventral retinal injections labeled projections terminating in the posterior, anterior, ventral, and dorsal tectal neuropil, respectively (Figures 6A–6D). This analysis also revealed that five of the ten AFs receive nonuniform visual maps. AF6 is innervated more heavily by dorsal RGCs, whereas AF1, AF4, and AF8 are each preferentially innervated by ventrally located RGCs (Figure 6E). AF7 is the only AF predominantly innervated by temporal retina (Figure 6F and Movie S2). Therefore, a significant fraction of all retinal inputs (nine projection classes that represent 29% of RGCs) contribute to the formation of nonuniform visual maps in extratectal AFs.

To examine the cellular basis of these asymmetries, we analyzed the cell body position of RGCs with axonal projection patterns that form biased visual maps in the brain. We initially focused on PC2, an RGC population that should be overrepresented in temporal retina based on providing all input to AF7. This projection class originates from two dendritic classes: B2 bistratified and D1 diffuse RGCs (Figure 5B). To determine the average temperonasal position of RGCs in this projection class, we measured cell body positions relative to the temporal edge of the retina (Figure 6G). Analysis of the temperonasal position of each RGC in PC2 confirmed that these were predominantly located in temporal retina (n = 19; mean temperonasal position: 35.1 ± 5.7 μm; Figures 6H and 6I). In contrast, the total B2 and D1 populations exhibited a uniform distribution along the temperonasal axis (n = 100; mean temperonasal position: 62.4 ± 3.3 μm, p = 0.0008; Figures 6H and 6I). This suggests that axonal innervation of AF7 is a morphological feature specified within a temporal subpopulation of B2 and D1 RGCs in the retina. In the tectum, AF7-targeting B2 RGCs innervate the SO, whereas other B2 RGCs innervate the SFGS1 and SFGS3–SFGS6 layers (PC3 and PC6–PC9). Examination of axon arbor position in the tectum revealed that B2 RGCs that target the superficial layers of the tectum (SO and SFGS1; n = 21) preferentially innervate anterior tectum, whereas B2 RGCs targeting deeper layers (SFGS3–SFGS6; n = 26) preferentially innervate posterior tectum (Figures 6J–6L). Therefore, although the tectum receives retinal inputs spanning the entire visual field, individual sublaminae receive retinotopically biased inputs from specific RGC dendritic classes. Together, these data support a hierarchical model in which broad RGC types defined by dendritic morphology are subdivided by the topographic induction of projection-specific genetic programs.

The Retinal Projectome Reveals a Functional Subdivision of AF9

Spatial segregation of RGC inputs with different response properties has been demonstrated in several brain regions [15]. We theorized that it would be possible to identify functional subdivisions of AFs based solely on connectivity patterns revealed by the projectome. Projection mapping revealed that AF9 contains two nonoverlapping populations of retinal inputs with different tectal projection patterns and different dendritic morphologies. Class 14 axons target AF9 and terminate in the SGC, whereas classes 16–20 each target AF9 and terminate in SAC/SPV. Sixty percent of these SAC/SPV-terminating axons originate from RGCs with dendrites restricted to the ON layers of the IPL, whereas SGC-terminating AF9 axons are formed entirely by M1 monostratified OFF and B1 bistratified RGCs. To determine whether these inputs are routed through distinct subregions of AF9, we analyzed the position of these AF9 arbors relative to the dorsal edge of AF9. Arbors formed by SGC-terminating axons exhibited a more ventral position within AF9 compared to AF9 arbors

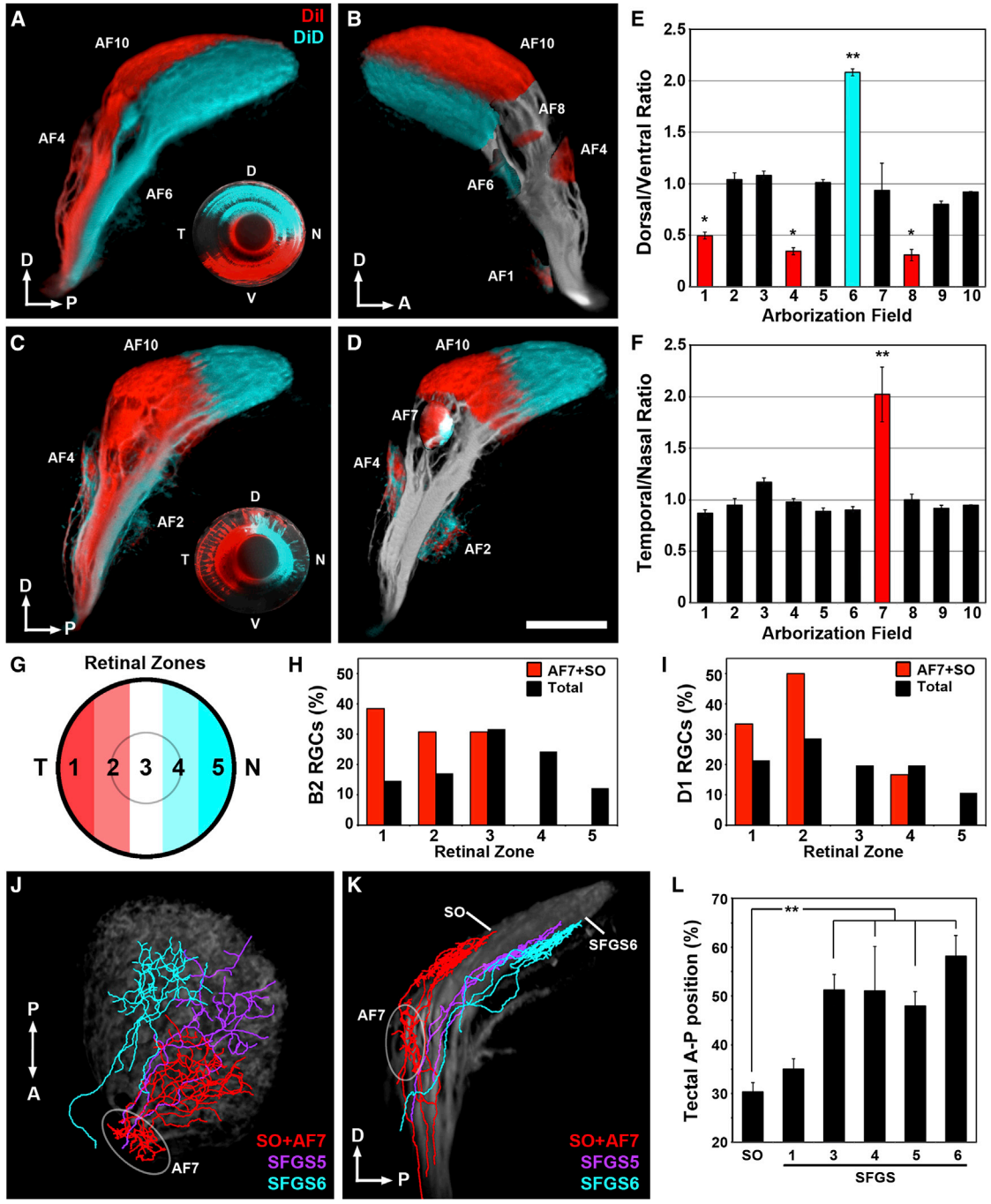

Figure 6. Nonuniform Distributions of RGC Types with Specific Projection Patterns Generate Biased Visual Maps in the Brain

(A) Lateral view of 7 dpf optic tract labeled by injection of DiI (red) and DiD (cyan) into ventral and dorsal hemiretinae. The inset shows the contralateral eye.

(B) A 180° rotation (medial view) of volume in (A). The optic tract in gray is superimposed with pseudocolored subvolumes of a subset of AFs. Note the disproportionate labeling of AF1, AF4, AF6, and AF8.

(C) Optic tract labeled by injection of DiI and DiD into nasal and temporal hemiretinae.

(D) Same volume as in (D). Note temporal bias of AF7 labeling.

(E and F) Quantification of relative AF area contributed by specified hemiretina. n = 5 for each axis.

(G) Schematic of nasotemporal zones used to analyze cell body position in the retina.

(H and I) Quantification of B2 and D1 RGC cell body positions for the AF7/SO subpopulation (red; n = 13 and 6) and all B2 and D1 cells (black; n = 44 and 56).

(J) Composite image of ten B2 axons 3D registered to the same tectum (shown in gray) and skeletonized. Four axons innervated AF7 and the SO sublamina of the tectum (red), two innervated SFGS5 (purple), and four innervated SFGS6 (cyan).

(K) Lateral view of volume in (J). Note that anterior position of superficially targeted axons and posterior position of axons targeted to deep SFGS.

(L) Quantification of anteroposterior position for B2 axons innervating SO or SFGS1, SFGS3, SFGS4, SFGS5, or SFGS6. *$p < 0.05$, **$p < 0.001$.

Data are presented as mean ± SEM (E, F, and L). Scale bars represent 65 μm (A–D) and 50 μm (J and K). See also Movie S2.

formed by SAC/SPV-terminating axons (14.2 ± 0.6 μm versus 5.6 ± 0.9 μm; $p < 0.0001$, $n \geq 8$). This difference in dorsoventral arbor position was confirmed by 3D-registering brain volumes containing single SAC/SPV or SGC-terminating AF9 axons to a reference optic tract volume (Figures 7A and S3). The dorsal main body of AF9 that receives SAC/SPV-terminating arbors will be referred to as AF9d, and the ventral region containing SGC-terminating arbors will be referred to as AF9v (Figure 7B).

AF9d-innervating RGCs predominantly originate from RGCs with dendrites restricted to the ON layers of the IPL, whereas SGC-terminating AF9 axons are formed by either M1 monostratified OFF or B1 bistratified RGCs. Therefore, dendritic morphology predicts that AF9d and AF9v subregions are functionally distinct, with AF9d axons responding to increases in luminance (ON responses) and AF9v axons predominantly responding to decreases in luminance (OFF responses). To test this prediction, we conducted multiphoton imaging in transgenic larvae with pan-RGC expression of the calcium indicator protein GCaMP6s during presentation of a 3 s white-screen stimulus. We monitored visual responses at two different z planes: (1) a dorsal plane of AF9, which includes only AF9d, and (2) a ventral plane of AF9, which includes AF9v and a region of AF9d at the posterior edge (Figure 7C). We were able to reliably detect responses in AF9 and classify regions of interest as ON, OFF, or ON-OFF (Figures 7D–7F). Functional imaging revealed that dorsal and ventral AF9 contain different proportions of ON- and OFF-responsive axon terminals. As predicted, the AF9d-containing dorsal plane predominantly consisted of ON axon terminals, whereas the ventral plane that includes AF9v contained similar proportions of ON- and OFF-responsive regions (Figure 7G and Movie S2). Although ventral AF9 contains a significant fraction of ON inputs, most of these were located in a region of AF9d that lies posterior to AF9v (Figures 7H and 7I). Together, these findings confirm the power of unbiased projection mapping to identify functional subdivisions of brain regions by virtue of divergent connectivity patterns.

Discussion

This study represents the first systematic, unbiased analysis of RGC axonal projections in a vertebrate. The 20 stereotyped projection patterns we have identified distinguish RGCs that transmit visual information to different brain regions and are therefore likely to subserve different functions. Our data set of 446 cells represents more than 10% of all RGCs in the 7 dpf zebrafish retina (approximately 4,000; E. Robles, unpublished data). Extrapolation estimates indicate that an increased sample size of 4,000 cells could reveal as many as 23 distinct projection patterns, suggesting that additional projection classes may exist. Based on projection class incidence, we estimate that the most numerous projection pattern (14%, PC7) is exhibited by 560 RGCs per retina, whereas the rarest (0.7%, PC16) is exhibited by 27 RGCs per retina.

Our findings clearly indicate that axonal projection patterns subdivide RGC classes defined by retinal features alone. By combining axonal and dendritic classifications, we have identified more than 50, and perhaps as many as 82, stereotyped morphological RGC types. Even a conservative estimate of 50 distinct RGC morphologies exceeds the number of cell types recognized so far in other vertebrates by a factor of two or three. However, our current count is most likely an underestimate, as many specific combinations were observed once or twice and could only be validated by increased sampling. In addition, we cannot exclude the possibility that individual types we have described may be further subdivided based on physiological response properties or gene expression profiles. It is crucial to note that RGCs with similar dendritic morphologies but different axonal projection patterns transmit information to different brain regions and are therefore likely to influence distinct aspects of visual behavior. Our finding that most dendritic classes of RGCs form multiple projection patterns is in agreement with the different projection patterns reported for ON-OFF direction-selective RGCs in the mouse [8–10]. Given the similarities between the larval zebrafish visual system and that of other nonprimate mammals (complex RGC projections innervating multiple brain areas and predominance of RGC axons terminating in the tectum/SC), it is likely that this general organizing principle is conserved in mammals. Application of a conservative estimate of four projection patterns per dendritic class to current estimates of RGC types in the mouse yields a total of more than 80 structural RGC types. However, mammalian visual systems contain more than 25 retinorecipient visual areas [12] and are therefore likely to contain an even greater diversity of projection patterns.

The prevalence of projection classes that innervate multiple brain regions suggests a prominent role for parallel processing strategies in generating visual behaviors. Studies in mammals have demonstrated that axonal branching is a common feature not only of retinal afferents, but also of projections between subcortical and cortical visual areas in mammals [35]. This may represent an evolutionary adaptation to minimize cellular material and energy required to broadcast the same information to multiple brain areas. RGC-type-specific axon branching ensures that select features of the visual scene are transmitted in parallel to circuits in the hypothalamus, thalamus, pretectum, and tectum. The simplest explanation is that the same sensory input may be utilized in different ways by these brain areas. For example, luminance information routed to AF1 in the hypothalamus could control circadian pacemaker functions, while this information might be used by the tectum to track objects against changes in ambient light level. Visual circuits receiving shared inputs may also exert modulatory effects on each other. The adult teleost brain contains three retinorecipient brain nuclei that provide afferent input to the tectum [13, 36]. In rodents, the suprachiasmatic nucleus and inner geniculate leaflet receive shared retinal inputs, are reciprocally connected, and regulate distinct aspects of circadian rhythmicity [37]. Future cell type analyses will be required to determine the interareal connectivity of retinorecipient nuclei.

The RGC diversity we have described is generated via cell-type-specific developmental programs controlling axonal and dendritic differentiation. Multiday imaging of the same cells showed that both dendritic and axonal patterns are stable during larval development. Previous studies have cataloged genes that label retinal neurons with specific stratification patterns in the IPL [38]. Cell-surface adhesion molecules belonging to the immunoglobulin-domain-containing superfamily (IgSF) influence dendritic branching patterns and synaptic connectivity in the IPL [39]. RGCs with identical dendritic stratification can differ widely in their axonal projections, which should be reflected in their gene expression patterns. For example, Cadherin-6 function is specifically required for proper innervation of two pretectal nuclei by a heterogeneous population of genetically defined RGCs [40]. It has also been shown that Reelin signaling is required for proper innervation of the vLGN by intrinsically photosensitive RGCs (ipRGCs) [41]. Together, these findings support the existence of genetic

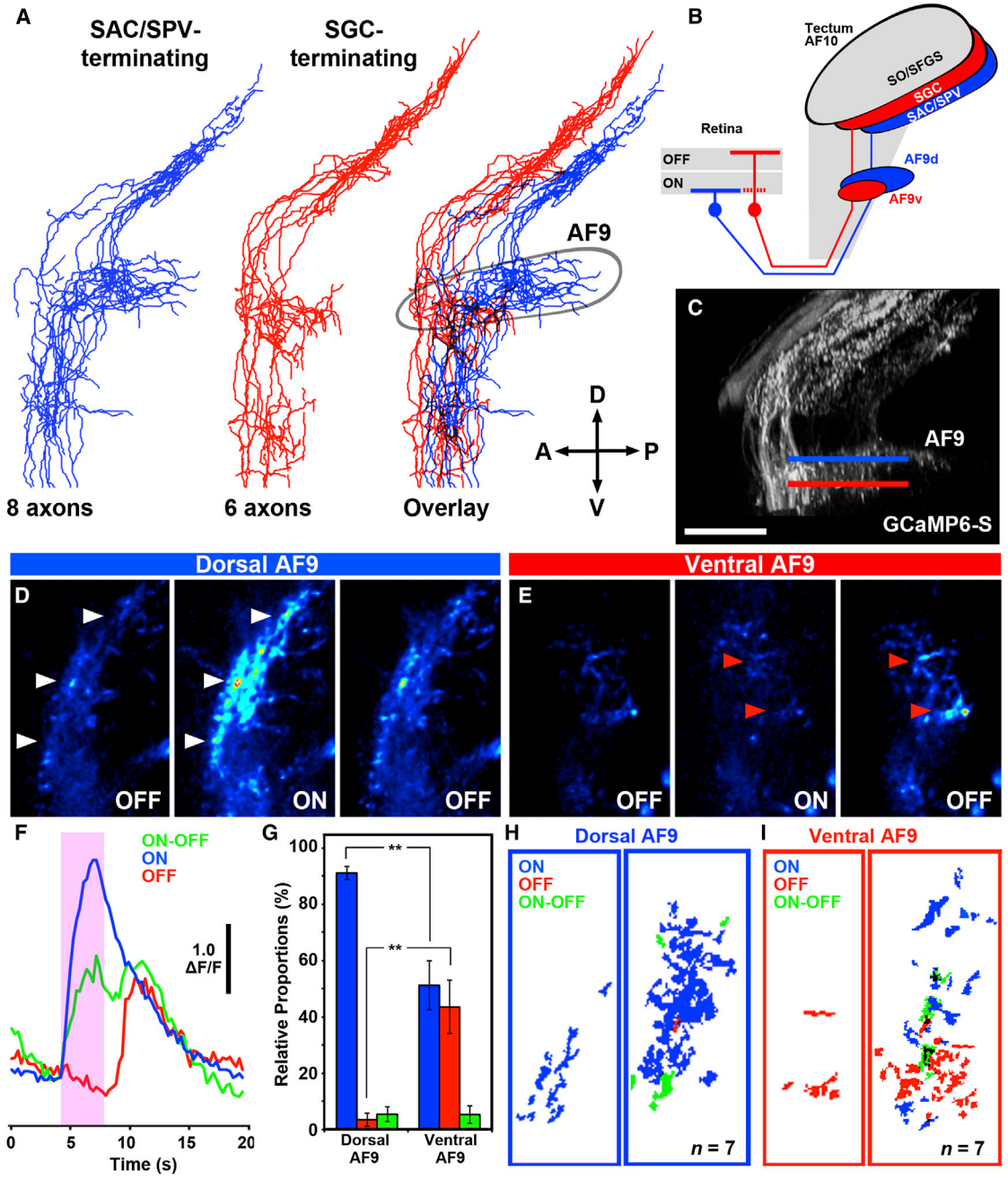

Figure 7. Anatomical and Functional Subdivision of AF9

(A) Lateral-view line tracings of eight SAC/SPV-terminating (blue) and six SGC-terminating (red) AF9 axons that were 3D registered to a reference optic tract. Note that the AF9 collaterals of SGC-terminating axons are formed anterior and ventral to the SAC/SPV-terminating collaterals.

(B) Schematic summarizing the distinct termination site and dendritic morphologies of AF9A- and AF9B-targeting RGCs.

(C) Optic tract labeled by pan-RGC expression of GCaMP6s. Blue and red lines indicate dorsal and ventral AF9 imaging planes.

(D) Single images of dorsal AF9 acquired immediately prior, during, and immediately after presentation of a 3 s white-screen stimulus to the contralateral eye. Arrowheads indicate areas responding at stimulus onset.

(E) Single images of ventral AF9. Red arrowheads indicate areas responding at stimulus offset.

(F) GCaMP6s fluorescence intensity traces of AF9 regions of interest (ROIs) classified as ON, OFF, or ON-OFF.

(G) Relative proportions of ON (blue), OFF (red), and ON-OFF (green) ROIs within dorsal and ventral AF9. Data are presented as mean ± SEM.

(H) Color-coded masks of dorsal AF9 ROIs classified as ON, OFF, or ON-OFF from either the image sequence in (D) (left) or an overlay of masks from seven different larvae (right).

(I) Color-coded masks of ventral AF9 ROIs classified as ON, OFF, or ON-OFF from image sequence in (E) (left) or overlay of seven larvae (right). Note that OFF ROIs predominantly cluster to an anterior/ventral AF9 region that corresponds to AF9B.

Scale bars represent 40 μm (C) and 25 μm (D and E). See also Movie S3.

programs that ensure RGC-type-specific targeting of each retinorecipient area. These signals likely act in a combinatorial fashion to generate complex patterns of AF and tectal layer innervation.

Cellular-resolution projection mapping allowed us to generate a model that explains how retinotopically biased visual maps in the brain are formed by RGC dendritic classes that are uniformly distributed in the retina. For example, a morphological survey restricted to the retina might interpret B2 RGCs as a single type evenly distributed throughout the retina, when in fact these cells form distinct projections based on their cell body position. Nonuniform visual map formation throughout the visual system may reflect a design principle aimed at minimizing the RGC number and axonal length required to transmit essential visual information to each AF. AFs that receive nonuniform visual maps may subserve functions that do not require accurate representation of the entire visual field. Routing of retinotopically biased visual information to specific brain areas may also confer ecological advantages. For example ventrally positioned RGCs may be ideally positioned for detection of overhead predators [42], whereas a temporal bias may be ideal for RGCs involved in tracking prey objects located in frontal eye fields. Although our data suggest that most biased visual maps in the brain are formed by topographic induction of distinct projection patterns, we cannot exclude that a subset of RGC dendritic classes may have nonuniform distributions. Recent studies in the mouse have identified a small subset of RGC subtypes with topographically biased distributions in the retina, M1 and M2 melanopsin-expressing ipRGCs [43], W3 RGCs [42], and alpha-like RGCs [44]. Our findings suggest that these genetically defined subpopulations may have arisen from more general classes of RGCs that are uniformly distributed in the retina. This is consistent with the finding that M1 and M2 ipRGC subtypes in the mouse are present in higher densities in dorsal retina, whereas ipRGCs as a whole are uniformly distributed [43]. We anticipate that several RGC types with uniform retinal distributions in mammals will prove to be subdivided into topographic subdomains with distinct central projection patterns.

Our findings confirm that a cellular-resolution projectome can illuminate organizational principles of sensory information transfer to the brain. A higher standard for neuroanatomical surveys is the ability to predict functional specialization of brain regions based on distinct connectivity patterns. In the olfactory system of *Drosophila*, comprehensive mapping of glomerular projection neuron terminals in the brain provided evidence for spatial segregation of food-related and pheromone-related odorant pathways [45]. These findings suggested that patterns of input connectivity can be used to identify brain areas involved in different sensory-evoked behaviors. Our unbiased projection mapping identified a functional subdivision of AF9 based on the distinct axonal and dendritic morphologies of their RGC inputs. AF9d and AF9v exhibit divergent functional responses to changes in luminance and may contribute to different visual behaviors. AF9d is mainly innervated by RGCs with dendrites stratified in the ON sublayer of the IPL, which is reminiscent of nuclei within the accessory optic system of mammals [46]. A recent study has identified populations of neurons located in close proximity to AF9d that process horizontal optic flow and are required for the optokinetic response, a behavior that compensates for self-motion [47]. Interestingly, the optokinetic response requires retinal ON signals and cannot be driven by OFF ganglion cells [48]. Taken together, these data suggest that AF9d and AF9v contribute to distinct visual behaviors, although the function of AF9v has yet to be determined.

In conclusion, the retinal projectome has generated a wiring diagram of retinal projections to the brain and illuminated several fundamental organizing principles of vertebrate visual systems. Our findings confirm the power of projection mapping to quantify cell type diversity and identify functional subdivisions of the brain. This map of visual inputs will provide a blueprint for functional imaging studies aimed at characterizing sensory and motor processes downstream of RGCs.

Experimental Procedures

Fish Lines

All animal procedures conformed to a protocol approved by the local government agency. The previously described transgenic lines used in this study are as follows: *Tg(isl2b:Gal4-VP16)*, *Tg(atoh7:Gal4-VP16)*, *Tg(14xUAS-mCherry-MA)*, *Tg(14xUAS:UAS:syn-GFP)*, and *BGUG Tg(brn3c:GAL4, UAS:gap43-GFP)s318t*. The mutant lines used were *mitfa*$^{-/-}$ *(nacre)* and *roy*$^{-/-}$. The *Tg(14xUAS-GCAMP6S)* transgenic line was generated by Tol2 transgenesis as previously described [21].

Image Acquisition

For live imaging, 6–7 dpf larvae were anesthetized in 0.016% tricaine and embedded in 2% low-melting-point agarose. Imaging was performed on a Carl Zeiss LSM-780 confocal microscope equipped with lasers for excitation of EGFP (488 nm) and mCherry (543 nm). Optical sections were acquired using 1 μm z steps. Vibratome sectioning and immunofluorescence staining was performed as previously described [21]. For calcium imaging, 7 dpf *Tg(isl2b:Gal4, 14xUAS-GCAMP6S)* nacre larvae were imaged using a custom-built two-photon microscope equipped with a mode-locked Ti:Sapphire Chameleon UltraII laser (Coherent) tuned to 920 nm.

Image Analysis

Image analysis was performed using ImageJ FIJI software. 3D rendering and volume clipping was performed with the 3D Viewer FIJI plugin developed by B. Schmid (University of Würzburg). Semiautomated axon segmentation was performed with the Simple Neurite Tracer FIJI plugin. 3D registration of image volumes was performed with VAA3D software developed by the laboratory of H. Peng (Allen Brain Institute).

Detailed methods are available in the Supplemental Experimental Procedures.

Supplemental Information

Supplemental Information includes Supplemental Experimental Procedures, six figures, two tables, and three movies and can be found with this article online at http://dx.doi.org/10.1016/j.cub.2014.07.080.

Author Contributions

E.R. and H.B. designed the experiments. E.R. and E.L. performed the experiments and analyzed data. E.R, E.L., and H.B. wrote the paper.

Acknowledgments

This work was supported by the Max Planck Society. We are grateful to Moritz Helmstaedter, Julie Semmelhack, Tod Thiele, Fumi Kubo, and Marco Dal Maschio for critical reading of the manuscript and to Leanne Godinho for helpful discussions and technical assistance.

Received: July 29, 2014
Revised: July 29, 2014
Accepted: July 31, 2014
Published: August 21, 2014

References

1. Badea, T.C., and Nathans, J. (2004). Quantitative analysis of neuronal morphologies in the mouse retina visualized by using a genetically directed reporter. J. Comp. Neurol. *480*, 331–351.

2. Kong, J.-H., Fish, D.R., Rockhill, R.L., and Masland, R.H. (2005). Diversity of ganglion cells in the mouse retina: unsupervised morphological classification and its limits. J. Comp. Neurol. *489*, 293–310.
3. Rockhill, R.L., Daly, F.J., MacNeil, M.A., Brown, S.P., and Masland, R.H. (2002). The diversity of ganglion cells in a mammalian retina. J. Neurosci. *22*, 3831–3843.
4. Roska, B., and Werblin, F. (2001). Vertical interactions across ten parallel, stacked representations in the mammalian retina. Nature *410*, 583–587.
5. Sümbül, U., Song, S., McCulloch, K., Becker, M., Lin, B., Sanes, J.R., Masland, R.H., and Seung, H.S. (2014). A genetic and computational approach to structurally classify neuronal types. Nat. Commun. *5*, 3512.
6. Völgyi, B., Chheda, S., and Bloomfield, S.A. (2009). Tracer coupling patterns of the ganglion cell subtypes in the mouse retina. J. Comp. Neurol. *512*, 664–687.
7. Roska, B., and Meister, M. (2014). The retina dissects the visual scene into distinct features. In The New Visual Neurosciences, J.S. Werner and L.M. Calupa, eds. (Cambridge: MIT Press), pp. 163–182.
8. Rivlin-Etzion, M., Zhou, K., Wei, W., Elstrott, J., Nguyen, P.L., Barres, B.A., Huberman, A.D., and Feller, M.B. (2011). Transgenic mice reveal unexpected diversity of on-off direction-selective retinal ganglion cell subtypes and brain structures involved in motion processing. J. Neurosci. *31*, 8760–8769.
9. Kay, J.N., De la Huerta, I., Kim, I.-J., Zhang, Y., Yamagata, M., Chu, M.W., Meister, M., and Sanes, J.R. (2011). Retinal ganglion cells with distinct directional preferences differ in molecular identity, structure, and central projections. J. Neurosci. *31*, 7753–7762.
10. Dhande, O.S., Estevez, M.E., Quattrochi, L.E., El-Danaf, R.N., Nguyen, P.L., Berson, D.M., and Huberman, A.D. (2013). Genetic dissection of retinal inputs to brainstem nuclei controlling image stabilization. J. Neurosci. *33*, 17797–17813.
11. Berson, D.M. (2008). Retinal ganglion cell types and their central projections. In The Senses: A Comprehensive Reference, *Volume 1*, Basbaum, A.I., Kaneko, A., Shepherd, G.M., and Westheimer, G., eds. (San Diego: Academic Press), pp. 491–520.
12. Ling, C., Schneider, G.E., and Jhaveri, S. (1998). Target-specific morphology of retinal axon arbors in the adult hamster. Vis. Neurosci. *15*, 559–579.
13. Fraley, S.M., and Sharma, S.C. (1984). Topography of retinal axons in the diencephalon of goldfish. Cell Tissue Res. *238*, 529–538.
14. Meek, H.J. (1990). Tectal morphology: connections, neurones and synapses. In The Visual System of Fish, R. Douglas and M. Djamgoz, eds. (London: Springer Netherlands), pp. 239–277.
15. Dhande, O.S., and Huberman, A.D. (2014). Retinal ganglion cell maps in the brain: implications for visual processing. Curr. Opin. Neurobiol. *24*, 133–142.
16. Bowling, D.B., and Michael, C.R. (1980). Projection patterns of single physiologically characterized optic tract fibres in cat. Nature *286*, 899–902.
17. Stirling, R.V., and Merrill, E.G. (1987). Functional morphology of frog retinal ganglion cells and their central projections: the dimming detectors. J. Comp. Neurol. *258*, 477–495.
18. Tamamaki, N., Uhlrich, D.J., and Sherman, S.M. (1995). Morphology of physiologically identified retinal X and Y axons in the cat's thalamus and midbrain as revealed by intraaxonal injection of biocytin. J. Comp. Neurol. *354*, 583–607.
19. Wiggers, W. (1999). Projections of single retinal ganglion cells to the visual centers: an intracellular staining study in a plethodontid salamander. Vis. Neurosci. *16*, 435–447.
20. Springer, A.D., and Mednick, A.S. (1985). A quantitative study of the relative contribution of different retinal sectors to the innervation of various thalamic and pretectal nuclei in goldfish. J. Comp. Neurol. *242*, 369–380.
21. Robles, E., Filosa, A., and Baier, H. (2013). Precise lamination of retinal axons generates multiple parallel input pathways in the tectum. J. Neurosci. *33*, 5027–5039.
22. Xiao, T., and Baier, H. (2007). Lamina-specific axonal projections in the zebrafish tectum require the type IV collagen Dragnet. Nat. Neurosci. *10*, 1529–1537.
23. Antinucci, P., Nikolaou, N., Meyer, M.P., and Hindges, R. (2013). Teneurin-3 specifies morphological and functional connectivity of retinal ganglion cells in the vertebrate visual system. Cell Rep. *5*, 582–592.
24. Mangrum, W.I., Dowling, J.E., and Cohen, E.D. (2002). A morphological classification of ganglion cells in the zebrafish retina. Vis. Neurosci. *19*, 767–779.
25. Burrill, J.D., and Easter, S.S., Jr. (1994). Development of the retinofugal projections in the embryonic and larval zebrafish (Brachydanio rerio). J. Comp. Neurol. *346*, 583–600.
26. Meyer, M.P., and Smith, S.J. (2006). Evidence from in vivo imaging that synaptogenesis guides the growth and branching of axonal arbors by two distinct mechanisms. J. Neurosci. *26*, 3604–3614.
27. Linden, R., and Perry, V.H. (1983). Massive retinotectal projection in rats. Brain Res. *272*, 145–149.
28. Vaney, D.I., Peichl, L., Wässle, H., and Illing, R.B. (1981). Almost all ganglion cells in the rabbit retina project to the superior colliculus. Brain Res. *212*, 447–453.
29. Mumm, J.S., Williams, P.R., Godinho, L., Koerber, A., Pittman, A.J., Roeser, T., Chien, C.-B., Baier, H., and Wong, R.O.L. (2006). In vivo imaging reveals dendritic targeting of laminated afferents by zebrafish retinal ganglion cells. Neuron *52*, 609–621.
30. Jakobs, T.C., Koizumi, A., and Masland, R.H. (2008). The spatial distribution of glutamatergic inputs to dendrites of retinal ganglion cells. J. Comp. Neurol. *510*, 221–236.
31. Nevin, L.M., Taylor, M.R., and Baier, H. (2008). Hardwiring of fine synaptic layers in the zebrafish visual pathway. Neural Dev. *3*, 36.
32. Cook, J.E., Kondrashev, S.L., and Podugolnikova, T.A. (1996). Biplexiform ganglion cells, characterized by dendrites in both outer and inner plexiform layers, are regular, mosaic-forming elements of teleost fish retinae. Vis. Neurosci. *13*, 517–528.
33. Mariani, A.P. (1982). Biplexiform cells: ganglion cells of the primate retina that contact photoreceptors. Science *216*, 1134–1136.
34. Ramoa, A.S., Campbell, G., and Shatz, C.J. (1989). Retinal ganglion beta cells project transiently to the superior colliculus during development. Proc. Natl. Acad. Sci. USA *86*, 2061–2065.
35. Bullier, J., and Kennedy, H. (1987). Axonal bifurcation in the visual system. Trends Neurosci. *10*, 205–210.
36. Grover, B.G., and Sharma, S.C. (1981). Organization of extrinsic tectal connections in Goldfish (Caraccius auratus). J. Comp. Neurol. *196*, 471–488.
37. Morin, L.P., and Allen, C.N. (2006). The circadian visual system, 2005. Brain Res. Brain Res. Rev. *51*, 1–60.
38. Siegert, S., Scherf, B.G., Del Punta, K., Didkovsky, N., Heintz, N., and Roska, B. (2009). Genetic address book for retinal cell types. Nat. Neurosci. *12*, 1197–1204.
39. Sanes, J.R., and Yamagata, M. (2009). Many paths to synaptic specificity. Annu. Rev. Cell Dev. Biol. *25*, 161–195.
40. Osterhout, J.A., Josten, N., Yamada, J., Pan, F., Wu, S.W., Nguyen, P.L., Panagiotakos, G., Inoue, Y.U., Egusa, S.F., Volgyi, B., et al. (2011). Cadherin-6 mediates axon-target matching in a non-image-forming visual circuit. Neuron *71*, 632–639.
41. Su, J., Haner, C.V., Imbery, T.E., Brooks, J.M., Morhardt, D.R., Gorse, K., Guido, W., and Fox, M.A. (2011). Reelin is required for class-specific retinogeniculate targeting. J. Neurosci. *31*, 575–586.
42. Zhang, Y., Kim, I.-J., Sanes, J.R., and Meister, M. (2012). The most numerous ganglion cell type of the mouse retina is a selective feature detector. Proc. Natl. Acad. Sci. USA *109*, E2391–E2398.
43. Hughes, S., Watson, T.S., Foster, R.G., Peirson, S.N., and Hankins, M.W. (2013). Nonuniform distribution and spectral tuning of photosensitive retinal ganglion cells of the mouse retina. Curr. Biol. *23*, 1696–1701.
44. Bleckert, A., Schwartz, G.W., Turner, M.H., Rieke, F., and Wong, R.O.L. (2014). Visual space is represented by nonmatching topographies of distinct mouse retinal ganglion cell types. Curr. Biol. *24*, 310–315.
45. Jefferis, G.S.X.E., Potter, C.J., Chan, A.M., Marin, E.C., Rohlfing, T., Maurer, C.R., Jr., and Luo, L. (2007). Comprehensive maps of Drosophila higher olfactory centers: spatially segregated fruit and pheromone representation. Cell *128*, 1187–1203.
46. Buhl, E.H., and Peichl, L. (1986). Morphology of rabbit retinal ganglion cells projecting to the medial terminal nucleus of the accessory optic system. J. Comp. Neurol. *253*, 163–174.
47. Kubo, F., Hablitzel, B., Dal Maschio, M., Driever, W., Baier, H., and Arrenberg, A.B. (2014). Functional architecture of an optic flow-responsive area that drives horizontal eye movements in zebrafish. Neuron *81*, 1344–1359.
48. Emran, F., Rihel, J., Adolph, A.R., Wong, K.Y., Kraves, S., and Dowling, J.E. (2007). OFF ganglion cells cannot drive the optokinetic reflex in zebrafish. Proc. Natl. Acad. Sci. USA *104*, 19126–19131.